atmosphere

MDPI

Article

Wind Analysis of Typhoon Jebi (T1821) Based on High-Resolution WRF-LES Simulation

Tao Tao [1,2,*], Bingjian Hao [2], Jinbo Zheng [2] and Qingsong Zhang [2]

[1] Engineering Research Center of Anhui Green Building and Digital Construction, Anhui Polytechnic University, Wuhu 241000, China
[2] School of Architecture and Civil Engineering, Anhui Polytechnic University, Wuhu 241000, China
* Correspondence: taotao@mail.ahpu.edu.cn

Abstract

This study investigates the performance of a high-resolution Weather Research and Forecasting with large-eddy simulation (WRF-LES) model in simulating the strong wind of a realistic typhoon (Jebi, 2018). Multiple domains are nested to downscale the grid resolution from 4.5 km to 33.3 m, and grid size sensitivity is tested in the innermost WRF-LES domain. The commonly used 1.5-order turbulent kinetic energy (TKE) subgrid-scale (SGS) model is excessively dissipative near the ground; this causes overshoot in the mean velocity profile compared with the expected log-law profile, a phenomenon slightly amplified by finer grids. Horizontal roll structures in the typhoon boundary can be effectively resolved with the 100 m horizontal grid size (Δx). However, higher resolution is needed to capture small-scale turbulence, and the effective mesh resolution for resolved turbulence is about 5–9Δx near the ground. The nonlinear backscatter and anisotropy (NBA) model significantly reduces the overshoot, and the resolved velocity structures are insensitive to the SGS model except for the lowest model level.

Keywords: WRF-LES; typhoon boundary layer; subgrid-scale model; turbulence

1. Introduction

Meteorological models have been increasingly applied at sub-kilometer scales since the beginning of the 21st century, driven by advancements in computational capabilities [1]. The Weather Research and Forecasting (WRF) model, an open-source community model, is widely employed for such applications. At these fine scales, turbulence parameterization within WRF is typically implemented within a large-eddy simulation framework (hereafter WRF-LES). In most investigations employing WRF-LES, researchers have focused on idealized atmospheric boundary layer (ABL) flows [2–5] or realistic conditions characterized by moderate winds [1,6–8]. In contrast, the performance of WRF-LES under realistic strong-wind conditions, particularly within the typhoon boundary layer (TBL), remains largely unexamined.

Understanding wind characteristics in the TBL requires the consideration of both meteorological forcing and turbulent processes. Contemporary meteorological simulations are often constrained by coarse grid resolutions, emphasizing flow features at scales larger than turbulent motions. For instance, coherent structures such as horizontal roll vortices (HRSs) are known to be prevalent within the TBL [9,10] and have been linked to surface wind gusts [11,12]. At smaller scales, turbulent structures within the TBL also exhibit significant variability and contribute to gust generation [13]. In high-resolution computational fluid

Academic Editors: Ng Yin Kwee, Mohan Kumar Gajendran, Ijaz Fazil Syed Ahmed Kabir and Amirfarhang Mehdizadeh

Received: 21 December 2025
Revised: 16 January 2026
Accepted: 19 January 2026
Published: 21 January 2026

dynamics (CFD) simulations [14–16], researchers have identified large wind gust factors (exceeding 2) within urban canopies embedded in TBLs, which were primarily attributed to building-induced effects. However, these simulations typically prescribe inflow conditions using fixed wind profiles, thereby neglecting the evolution of meteorological-scale flows.

Seamlessly nested within real-time atmospheric simulations, WRF-LES incorporates realistic meteorological forcing while employing grid spacings of tens of meters or less to explicitly resolve turbulent motions [17]. Despite this potential, applications of WRF-LES to tropical cyclones remain scarce. Zhu (2008) [18] simulated Hurricane Katrina using WRF-LES and proposed a parameterization scheme for vertical turbulent transport that accounted for HRS effects. However, with a horizontal grid spacing (Δx) of 100 m, most resolved wind fluctuations were attributed to HRSs rather than smaller-scale turbulence.

Recent studies underscore both the capabilities and challenges of high-resolution WRF-LES for typhoon wind fields. For example, Liu et al. [19] demonstrated that horizontal grid resolutions finer than 100 m are necessary to resolve coherent turbulent structures such as boundary layer rolls and tornado-scale vortices within the TBL, whereas coarser resolutions within the "gray zone" [20] fail to capture these features. This highlights the critical role of grid resolution. Furthermore, physical parameterization significantly impacts accuracy. Takahashi et al. [21] showed that surface roughness length and planetary boundary layer (PBL) schemes in WRF substantially influence near-surface wind speed and vortex structure during typhoon landfall, indicating a need for observational constraints. For urban-scale applications, coupled mesoscale–microscale frameworks have been developed to predict building-scale winds during typhoons [22], and data assimilation techniques have been proposed to correct near-surface wind speed biases [23]. Collectively, these advancements represent more integrated and observationally informed approaches. However, the performance of subgrid-scale (SGS) models under extreme wind conditions and their impact on near-surface profiles require further evaluation.

This study aims to evaluate the performance of a high-resolution WRF-LES configuration in resolving strong-wind characteristics within the TBL of a real typhoon. The target event is Typhoon Jebi (T1821), which struck western Japan on 4 September 2018 and set records for maximum wind speeds in several cities [16]. The numerical configuration is described in Section 2. Resolved wind characteristics across different grid resolutions are presented in Section 3, followed by conclusions in Section 4.

2. Numerical Settings

The WRF model (version 3.7.1) [24] is configured with four one-way nested domains. The horizontal grid spacings (Δx) for the outermost three domains (D1, D2, and D3) are 4.5 km, 1.5 km, and 300 m, respectively. A fourth domain (D4) is nested within D3, centered on the city of Osaka. To investigate the influence of grid resolution, three simulations are conducted for D4 with Δx = 100 m, 60 m, and 33.33 m, hereafter referred to as D4-100 m, D4-60 m, and D4-33 m, respectively. In D1 and D2, the Yonsei University (YSU) [25] PBL parameterization scheme is used, while in D3 and D4, the SGS effects are modeled using LESs, with a standard 1.5-order turbulent kinetic energy (TKE) closure scheme [26] instead of the PBL scheme. This TKE-based SGS model is commonly employed in contemporary turbulence-resolving meteorological simulations [27–29]. For simplicity, D1 and D2 are termed WRF domains, while D3 and D4 are termed WRF-LES domains. The large grid ratio (5:1) between D2 and D3 helps mitigate the gray zone problem [20]. When the grid size (from about 300 to about 1000 m) is between the LES upper limit (slightly less than the integral turbulence scale) and the mesoscale lower limit (no resolved turbulence), there is no appropriate turbulence model or parameterization scheme. Domain locations and dimensions are provided in Figure 1 and Table 1. For consistency and computational

efficiency, domains D1 to D3 share an identical vertical coordinate system comprising 62 levels, with the lowest vertical grid spacing fixed at 40 m, a resolution commonly used in mesoscale WRF simulations. Within D4, vertical levels below 160 m above ground level (AGL) are refined, with spacings of 20 m, 10 m, and 5 m for D4-100 m, D4-60 m, and D4-33 m, respectively.

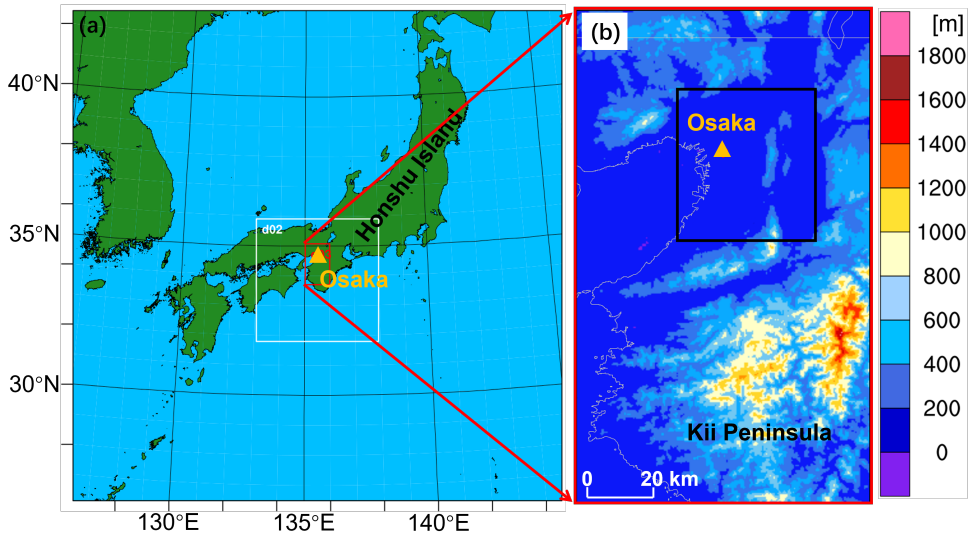

Figure 1. The WRF domains of the Typhoon Jebi simulation: (**a**) D1, D2, and D3. (**b**) The terrain height of D3, where the black rectangle shows the location of D4, and the orange triangle marker denotes the Osaka AMeDAS.

Table 1. Configuration of domains and grids in the simulation.

Domain ID	Horizontal Grid Size (m)	Duration (Sep 2018, UTC)	Grid Number	Time Step (s)	Vertical Grid Size Near the Ground (m)
D1	4500	03_1800–04_1200	401 × 401 × 62	15	40
D2	1500	04_0000–04_0700	301 × 301 × 62	3	40
D3	300	04_0200–04_0700	301 × 501 × 62	1	40
D4-100 m	100	04_0400–04_0600	418 × 463 × 77	0.5	20
D4-60 m	60	04_0400–04_0600	696 × 771 × 81	0.2	10
D4-33 m	33.33	04_0400–04_0600	1252 × 1387 × 88	0.2	5

The initial and lateral boundary conditions of D1 (including velocity, temperature, moisture, and geopotential height) are derived from the Japan Meteorological Agency (JMA) mesoscale analysis data, available hourly at a 4 km horizontal resolution. Soil temperature, soil moisture, and sea surface temperature are derived from the National Centers for Environmental Prediction (NCEP) Global Forecast System (GFS) 0.25-degree data [30], which are updated every 6 h. Finally, topography and land-use data for D1–D3 are interpolated from a 100 m mesh dataset provided by the Geospatial Information Authority of Japan, and for D4, a 30 m mesh dataset from the Japan Aerospace Exploration Agency is used [31].

To obtain an accurate typhoon track, grid nudging is applied within D1 throughout the simulation, constraining the simulated large-scale flow for mesoscale analysis. Given the relatively high spatiotemporal resolution of the analysis data, a typhoon bogussing scheme is not employed. Additional physics parameterization approaches include the Morrison two-moment microphysics scheme [32], the Rapid Radiative Transfer Model for Global climate model (RRTMG) radiation scheme [33], the Noah land surface model [34], and the Revised MM5 Monin-Obukhov surface layer scheme [35].

3. Results

3.1. Overview of the Simulated Typhoon

Without nudging, the simulated typhoon track in D1 exhibited a westward deviation from observations, with landfall on Honshu Island being displaced by approximately 20 km west. Activating grid nudging significantly improved track agreement (Figure 2); therefore, D2 was nested from the nudged D1 simulation. This configuration was adopted for two primary reasons. First, while coarse-resolution global analysis data (e.g., NCEP GFS at 0.25 degrees) often require a typhoon bogussing scheme to correct an initially weak vortex and its erroneous track, the present study uses the higher-resolution (4 km) JMA mesoscale analysis for initial and boundary conditions, rendering bogussing unnecessary. Second, deactivating grid nudging in D1 led to the 20 km westward track error near landfall. This likely stems from residual inaccuracies in the initial vortex and insufficient spin-up time over the ocean (the D1 simulation started only about 10 h before the typhoon reached the study area). Rather than employing bogussing or conducting trial-and-error domain adjustments, grid nudging was chosen as an efficient and effective means to obtain an accurate storm track. We acknowledge that grid nudging introduces an artificial forcing term into the governing equations, which may create physical inconsistencies in the simulated typhoon wind field. Consequently, the role of D1 is deliberately limited to providing a realistic typhoon track for the inner domains, ensuring that the nested high-resolution simulations (D2–D4) are driven by a meteorologically consistent large-scale flow.

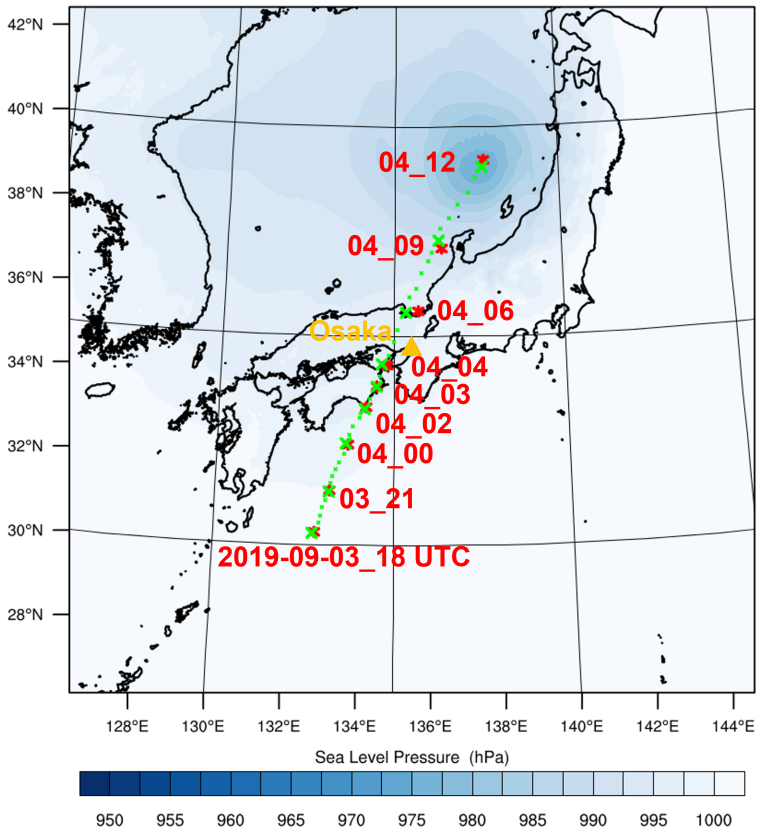

Figure 2. Typhoon tracks in D1. Simulated and observed tracks are shown in green and red markers, respectively. The orange triangle marker denotes the Osaka observation station. The filled color contour shows the sea-level pressure at 1200UTC, 04 Sep.

It is acknowledged that the one-way nesting approach used here does not allow for feedback from a nested domain to the parent domain, but this choice enhances computational efficiency and ensures that the large-scale forcing from the analysis data remains

consistent. For the purpose of this study, i.e., to evaluate the downscaling capability of WRF-LES under realistic meteorological forcing, the one-way framework is considered appropriate, as it preserves the integrity of the typhoon-scale circulation that drives inner-domain smaller-scale wind fluctuations.

The time series of wind speed at the Osaka observation station for all domains is shown in Figure 3. The temporal evolution of both wind direction and speed was consistent with the observations performed with the Automated Meteorological Data Acquisition System (AMeDAS). The maximum wind speed occurred at around 0510 UTC, and the wind direction was northward. Compared with D1 and D2, D3 displayed wind speeds with higher-frequency fluctuations (periods of approximately 1 min), indicating at least partial resolution of turbulence. Within the D4 domains, the resolved frequency content was further enhanced, with the highest frequencies increasing as the grid resolution was refined. Wind speeds were overestimated relative to observations across all domains, which may be partly attributed to an insufficient representation of urban roughness (prescribed as a constant 0.5 m in this study). This perspective is strongly supported by the findings obtained by Takahashi et al. [21], who adjusted the urban roughness length in WRF from the default value of 0.5 m to 2.0 m based on climatological data for urban and forest areas in Japan, thereby significantly mitigating the overestimation of near-surface wind speeds. The D4 domain in the present study is situated primarily around the city of Osaka, an area characterized by high building density and considerable structural height. Consequently, a roughness length of 0.5 m likely underestimates the actual surface roughness. However, while insufficient roughness length is a contributing factor, this study emphasizes an inherent limitation of the standard SGS model in WRF, which systematically leads to the overestimation of near-ground winds. Notably, this overestimation is amplified with finer grid resolutions in the D4 simulations, which will be further examined in the following subsection.

In addition to the Osaka AMeDAS station, model performance was also evaluated against observation data from six other AMeDAS stations located within the D4 domain (Hirakata, Ikoymayama, Yao, Kyotanabe, Toyonaka, and Sakai), as shown in Figure 4. All six stations exhibited wind speed histories qualitatively similar to that observed in Osaka. Statistical comparisons between simulated and observed 10 min average wind speeds across all seven stations are summarized in Table 2, which includes the Pearson correlation coefficient (ρ), mean bias (MB), mean absolute error (MAE), and root mean square error ($RMSE$), calculated as follows:

$$\rho(U, U^{obs}) = \frac{\sum_{i=1}^{N}(U_i - \overline{U})(U_i^{obs} - \overline{U^{obs}})}{\sqrt{\sum_{i=1}^{N}(U_i - \overline{U})^2 \sum_{i=1}^{N}(U_i^{obs} - \overline{U^{obs}})^2}}, \quad (1)$$

$$MB(U, U^{obs}) = \frac{1}{N}\sum_{i=1}^{N}(U_i - U_i^{obs}), \quad (2)$$

$$MAE(U, U^{obs}) = \frac{1}{N}\sum_{i=1}^{N}|U_i - U_i^{obs}|, \quad (3)$$

$$RMSE(U, U^{obs}) = \sqrt{\frac{1}{N}\sum_{i=1}^{N}(U_i - U_i^{obs})^2}, \quad (4)$$

where U and U^{obs} denote the model-simulated and observed 10 min average wind speed time series from 0500 to 0700 UTC.

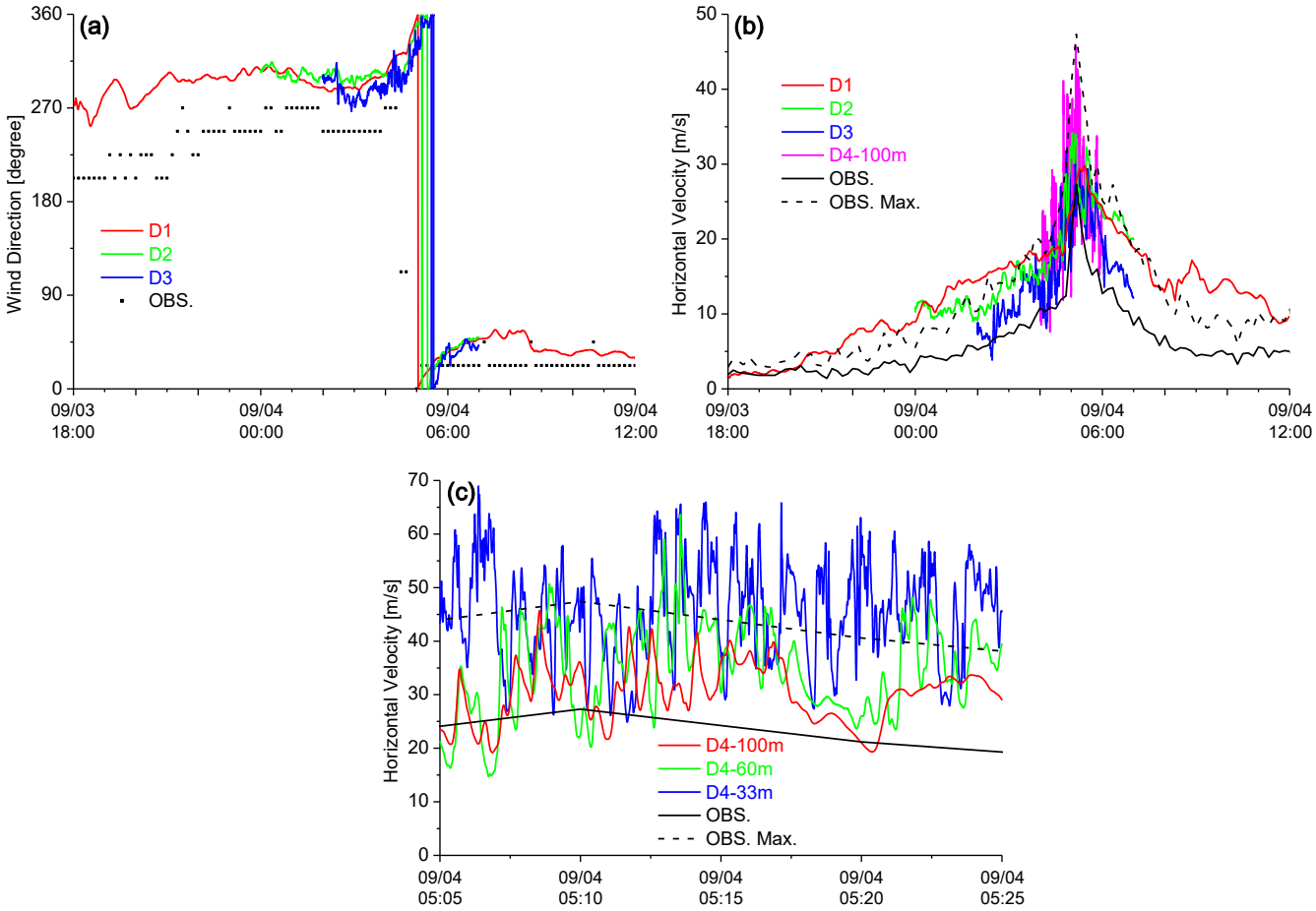

Figure 3. Simulated and observed wind velocity history for the Osaka AMeDAS observation station. The observation (OBS.) data are derived from the AMeDAS records. OBS. and OBS. Max. represent the 10 min averaged horizontal wind speed and maximum instantaneous horizontal speed within 10 min of the observation. The x-axis represents time in UTC. In (**a**,**b**), the time period is from 1800 on 3 September to 0700 on 4 September 2018. In (**a**), 0, 90, 180, and 270 degrees represent northward, eastward, southward, and westward wind directions. (**b**) shows the horizontal velocity magnitude in the whole simulation period. (**c**) shows the horizontal velocity magnitude of the D4 cases between 0505UTC and 0525UTC on 4 September 2018.

Table 2. Statistical comparison between the simulated and observed wind velocity at the AMeDAS observation stations at 0500–0700 UTC. Each value is the average of the values from the 7 AMeDAS stations (Osaka, Hirakata, Ikoymayama, Yao, Kyotanabe, Toyonaka, and Sakai). The unit of the values is m/s.

Domain ID	ρ	MB	MAE	RMSE	Average Gust Factor
D1	0.558	14.4	14.4	14.8	1.03
D2	0.485	14.9	14.9	15.6	1.06
D3	0.447	10.8	11.0	11.7	1.23
D4-100 m	0.502	5.24	6.42	6.96	1.44
D4-60 m	0.523	5.82	6.93	7.56	1.56
D4-33 m	0.476	10.0	10.4	11.0	1.68
AMeDAS					2.00

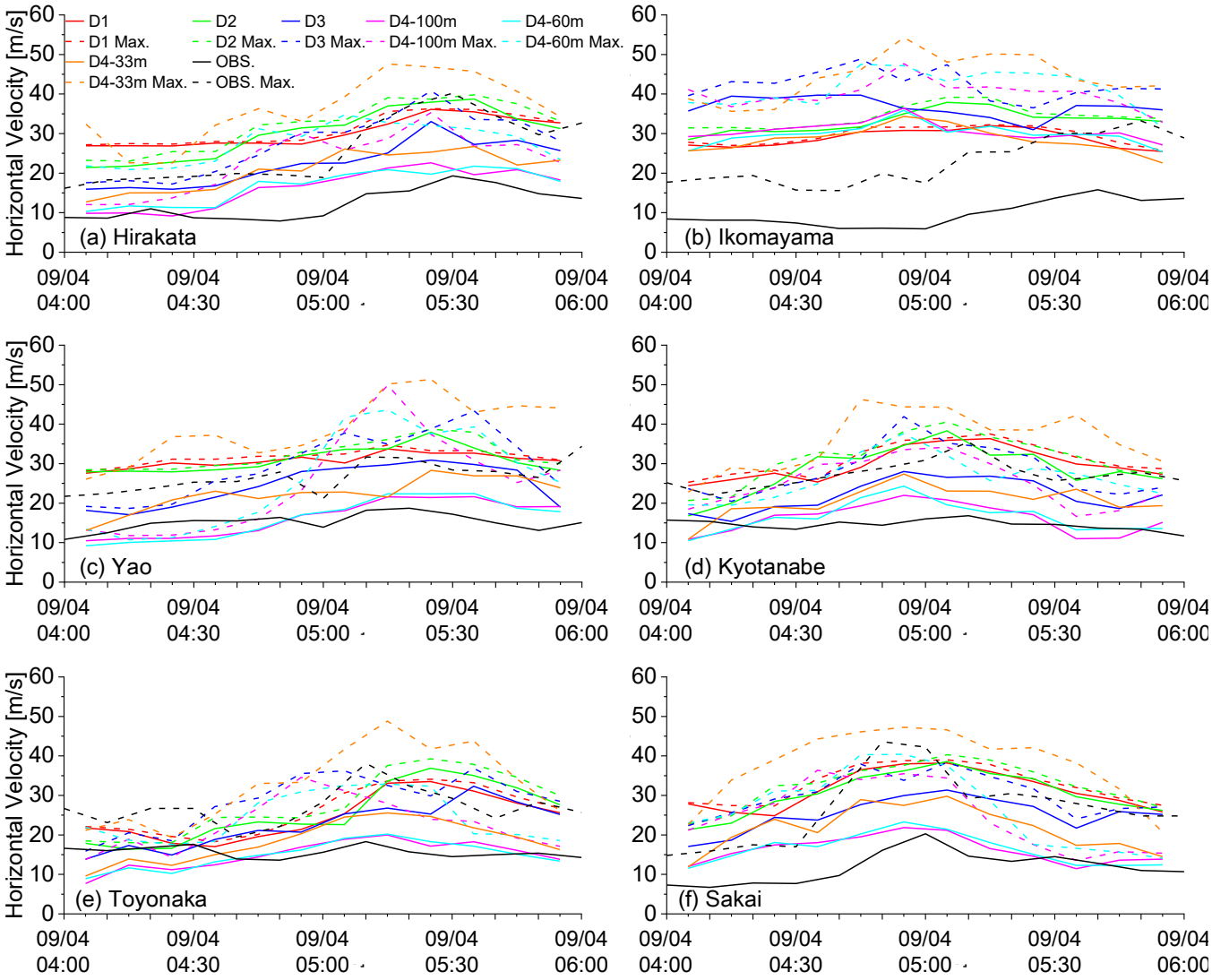

Figure 4. The 10 min averaged horizontal wind speed (solid lines) and maximum instantaneous horizontal speed within every 10-minute interval (dashed lines) of D1, D2, D3, D4 cases, and observations from AMeDAS stations (Hirakata, Ikoymayama, Yao, Kyotanabe, Toyonaka, and Sakai). The location of the stations is shown in Figure 5d.

Across most domains and stations, wind speeds are systematically overestimated. The overestimation is more pronounced in D1 (MB = 14.4 m/s) and D2 (MB = 14.9 m/s) than in D3 (MB = 10.8 m/s) and the D4 cases (MB ranging from 5.24 to 10.0 m/s). Among the D4 simulations, finer grid resolutions produce higher wind speeds, consistent with the earlier-reported findings from the Osaka AMeDAS station. Because overestimation persists throughout most of the period, MAE values are quantitatively similar to MB. In contrast, $RMES$ is more sensitive to localized biases. MAE and $RMES$ differ noticeably from MB only for D4-100 m and D4-60 m, where overestimation is weaker and occasional underestimation occurs.

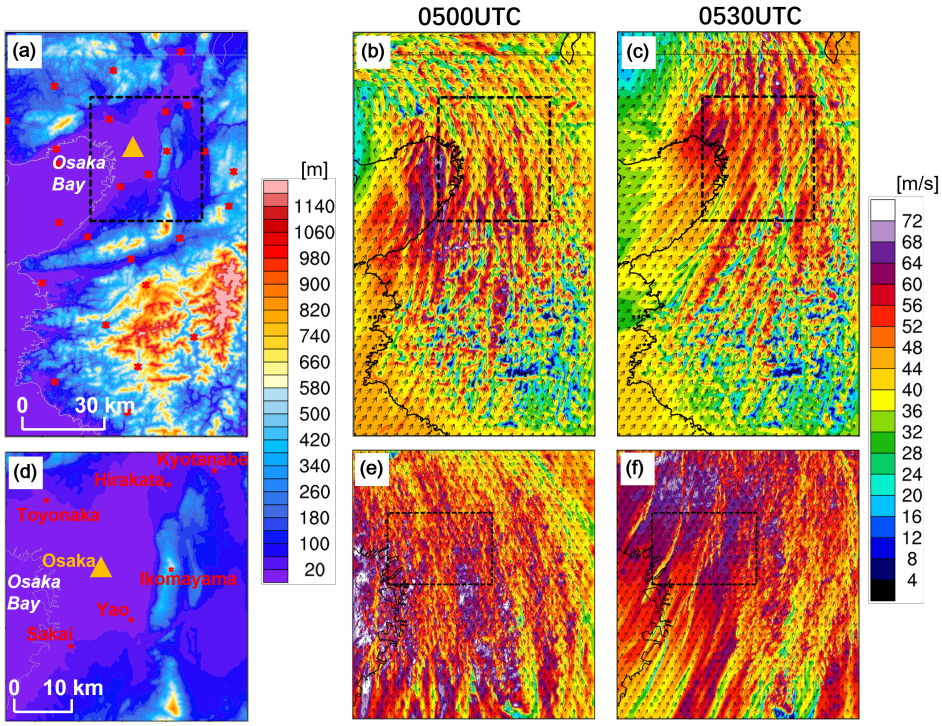

Figure 5. (**a**) The terrain of D3 and (**b**,**c**) the horizontal wind velocity at 200 m AGL at 0500UTC and 0530UTC on 4 September for WRFLES300m. (**d**–**f**) display the same data as in (**a**–**c**) but for D4-60 m. The dashed rectangle in (**a**–**c**) encloses the area of (**d**–**f**). The red dots denote the observation stations of the AMeDAS, except for the Osaka station, which is marked with an orange triangle. The dashed rectangle in (**e**,**f**) encloses the area referred to in Figures 6–8.

The correlation between simulated and observed wind speeds is moderate, with ρ values ranging from 0.476 to 0.558 across domains. This may be partly due to the short analysis window (two hours, from 0500 to 0700 UTC), during which the typhoon passed through the D4 region, and wind speeds remained near their peak, showing little systematic change. Instantaneous wind fluctuations increase with finer grid resolution, as reflected in the gust factors. The average gust factor derived from AMeDAS observations is 2.0, while the maximum simulated gust factor (1.68) occurs in D4-33 m. We attribute wind gusts primarily to turbulence within the atmospheric boundary layer. The underestimation of gust factors in the simulations may stem from two aspects: first, turbulence may not be fully developed in the model; second, D4-33 m substantially overestimates the mean wind speed, which can artificially reduce the gust factor.

A marked reduction in velocity fluctuations within D4 is observed after approximately 0517 UTC (Figure 3c). D4-100 m and D4-60 m show the weakening tendency clearly, while in D4-33 m, the latter is less discernible due to more high-frequency components. The examination of the horizontal wind field (Figure 5) reveals that at 0500 UTC, a southeasterly flow impinged on the mountainous Kii Peninsula, generating turbulent flow with relatively large fluctuations (Figure 5b). By 0530 UTC, the wind had shifted southwestward, traversing Osaka Bay, and the velocity fluctuations subsided significantly (Figure 5c). This suggests that upstream terrain undulation is conducive to turbulence generation, likely through vortex shedding in the wake of obstacles under strong-flow conditions.

3.2. Mean Wind Profile

Depicted in Figure 6, the mean wind profiles for the D4 cases were computed by averaging over an 18 km $\times$ 12 km area centered on the Osaka AMeDAS station to minimize the potential influence of local terrain differences among the cases. The terrain within this

area is relatively flat, with maximum undulations of approximately 20 m. Land use fields differ slightly due to differing grid resolutions, but differences in area-averaged surface roughness length are less than 2%, with a mean value of 0.449 m. The period of maximum wind speed (0505–0515 UTC) is chosen for the analysis. The time-averaged velocity is calculated with the 10 min window moving average, and the 3D wind field is saved from 0500 UTC to 0520 UTC with 1 s intervals.

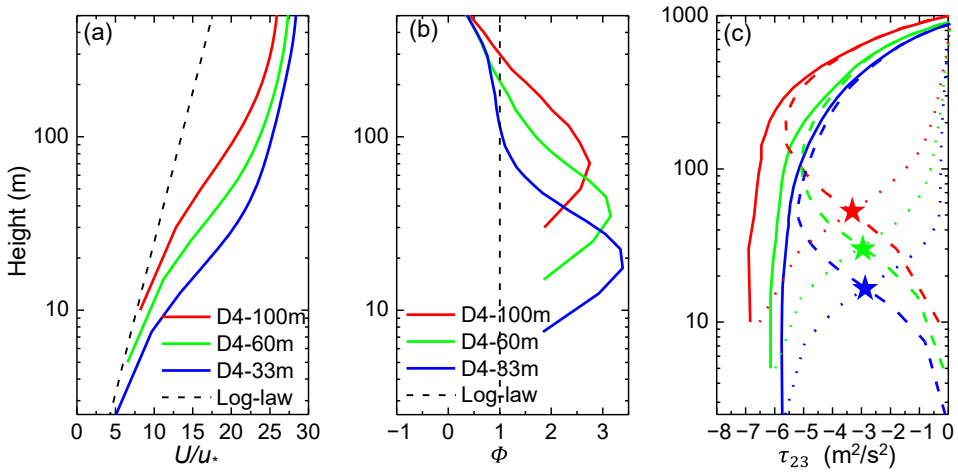

Figure 6. The vertical profiles of (**a**) normalized time-averaged horizontal speed, (**b**) nondimensional shear (Φ), and (**c**) shear stress on the north and vertical plane (τ_{23}). In (**a**), the log-law profile is based on neutral conditions. The profiles are the average profiles of model points in an 18 km × 12 km area centered on the Osaka AMeDAS. The time period is from 0505UTC to 0515UTC. The profiles for D4-100 m, D4-60 m, and D4-33 m are shown as red, green, and blue lines, respectively. In (**c**), the total, resolved, and SGS components are plotted as solid, dashed, and dotted lines, respectively. The pentagram indicates the location where the SGS and resolved components are equal. Note that the vertical coordinates are different in the panels.

From 0430 to 0600 UTC, the magnitude of the bulk Richardson number remained below 0.0015, indicating a nearly neutral atmosphere. The near-surface profile is compared with the theoretical logarithmic law (Figure 6a). We note that although the TBL is different from a typical turbulent boundary layer, herein, the log-law profile is considered an acceptable reference for the mean wind profile for two reasons: The target area is far away from the typhoon center; thus, the pressure gradient force and the influence of eyewall convection are relatively small. Further, surface drag is dominant at low levels owing to the strong wind. In all D4 cases, wind speeds overshoot the log-law prediction near the surface. This overshooting behavior associated with the 1.5-order TKE SGS model has been documented in prior studies [2–5]. When the grid scale is comparable to characteristic eddy sizes near the surface, the assumption that the filter scale lies within the inertial subrange is violated. The SGS model becomes excessively dissipative, underpredicting turbulent stress and consequently inducing excessive wind shear [36]. More advanced SGS models, such as the nonlinear backscatter and anisotropy (NBA) model [37], can mitigate such overshoot, as discussed later.

Nondimensional shear Φ is defined as

$$\Phi = (\kappa z / u_*)(\partial U / \partial z), \tag{5}$$

where κ is the von Kármán constant, z is the height, u_* is the friction velocity, and U is the mean horizontal wind. The profile of Φ (Figure 6b) indicates that the maximum Φ overshoot occurs at approximately the third level above the surface (more precisely, where

the SGS stress exceeds the resolved stress (Figure 6c), as shown by Brassur and Wei [36]). Such a Φ overshoot causes large wind velocity aloft. Thus, with finer grids, the deviation of the mean velocity profile from the theoretical log-law profile is larger. The total shear stress profiles show similar behaviors in all cases, except for the slightly smaller surface friction in finer cases (Figure 6c), which is consistent with the slightly larger wind shear.

The NBA model is tested as a replacement for the TKE model in the D4-60 m configuration (named D4-60 m NBA in the following figures). A comparison of profiles for the two SGS models is shown in Figure 7. The NBA model yields a significant improvement in the mean wind shear. The maximum Φ is reduced from 3.1 in the TKE model case to 1.6 in the NBA model. Both friction velocity and shear stress are larger in the NBA model than in the TKE model, confirming that insufficient turbulent stress is responsible for the overshooting problem. The NBA model also reduces the scale of stripe-like flow structures at the lowest scalar model level (5 m AGL), enhancing spectral power at higher wavenumbers (discussed in Sections 3.3 and 3.4). Above this level, differences in power spectra between the schemes are negligible. Therefore, the turbulent structures resolved by the TKE model above the lowest level are considered reasonable.

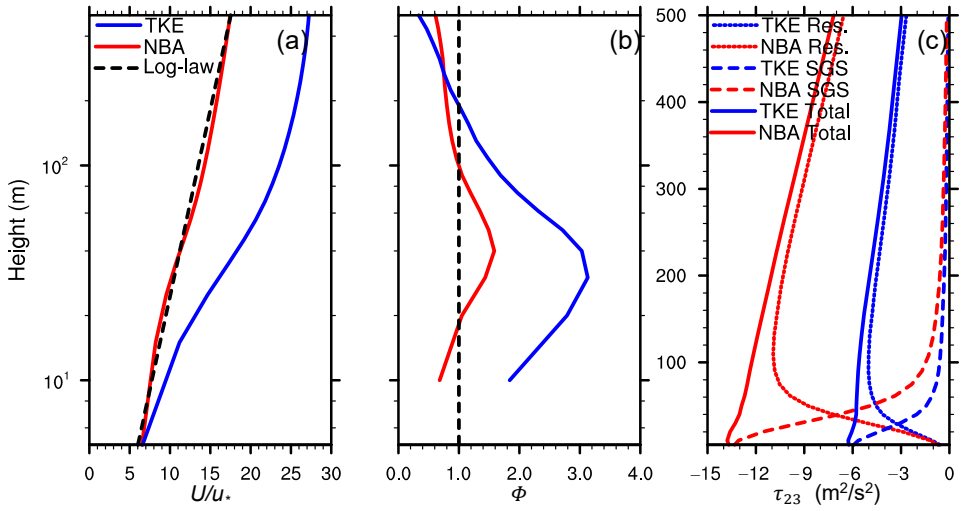

Figure 7. Same as Figure 6, except the plots refer to the standard 1.5-order TKE model and the NBA model for D4-60 m. Note that the vertical coordinate of (**c**) is different from those of (**a**,**b**).

3.3. Resolved Velocity Structures

To analyze the turbulent structures during the period with the most intense wind, a snapshot at 0510 UTC, which corresponds to the time when the peak wind speed at the Osaka AMeDAS station was observed (Figure 3c), is examined. The instantaneous wind field at 0510 UTC is presented in Figure 8. The analysis focuses on the northward wind component, which was dominant. Near the surface (30 m AGL), the turbulent velocity exhibits a stripe-like pattern aligned roughly with the mean wind direction. In the finer-resolution case (D4-33 m), the spacing between adjacent stripes is reduced, indicating the resolution of smaller-scale turbulent motions. These smaller-scale features are also identifiable at higher levels (200 and 400 m AGL), although their magnitude is less significant than that of larger-scale fluctuations, whose scale is similar across the D4 cases (around 1 km). Compared with the standard TKE run (D4-60 m), the NBA simulation (D4-60 m NBA) exhibits finer streaky structures with reduced spacing between adjacent streaks. This suggests that the NBA SGS model improves the representation of small-scale turbulent motions near the surface relative to the 1.5-order TKE closure scheme.

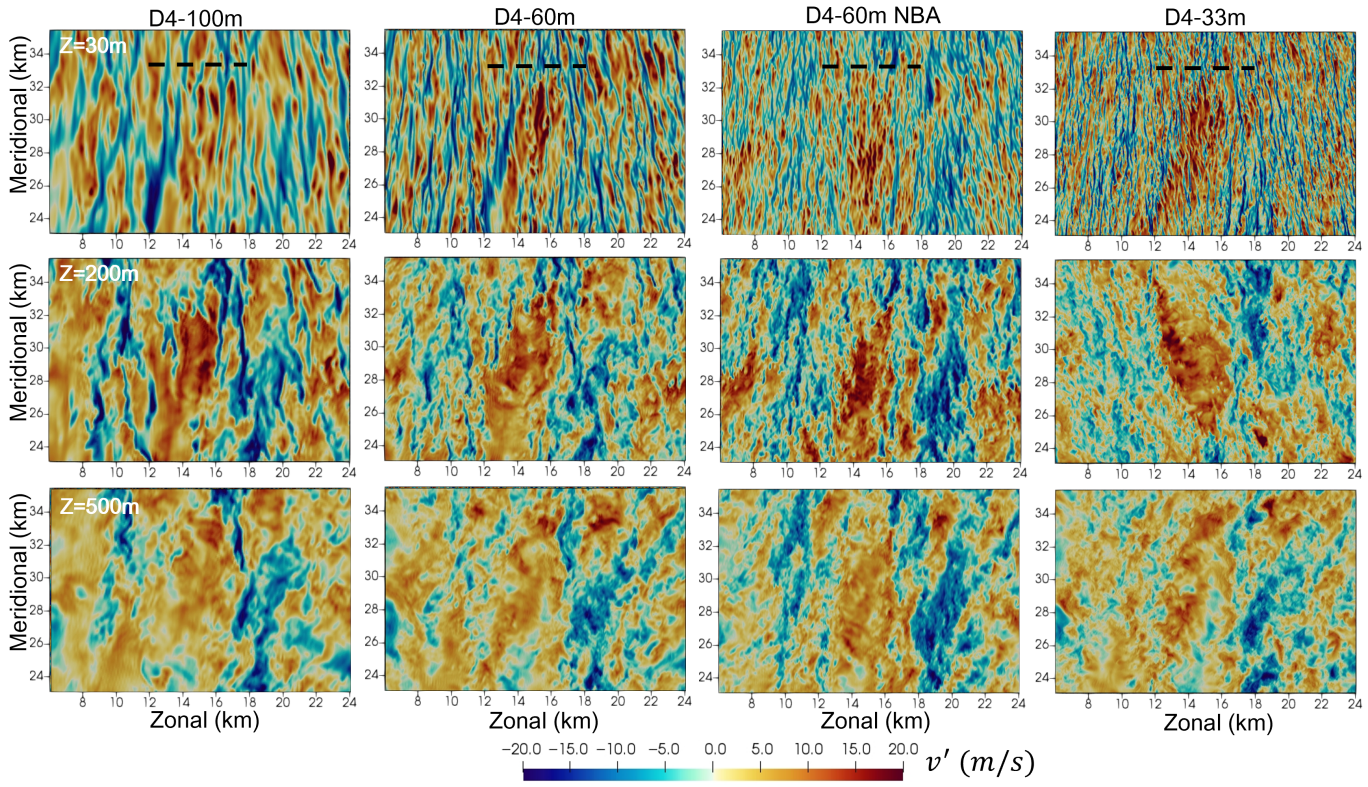

Figure 8. A snapshot of v' (the fluctuation component of the northward wind velocity) on the horizontal plane at different heights for the D4 cases. The time is 0510UTC. The dashed line shows the location of the vertical cross-section of Figure 9.

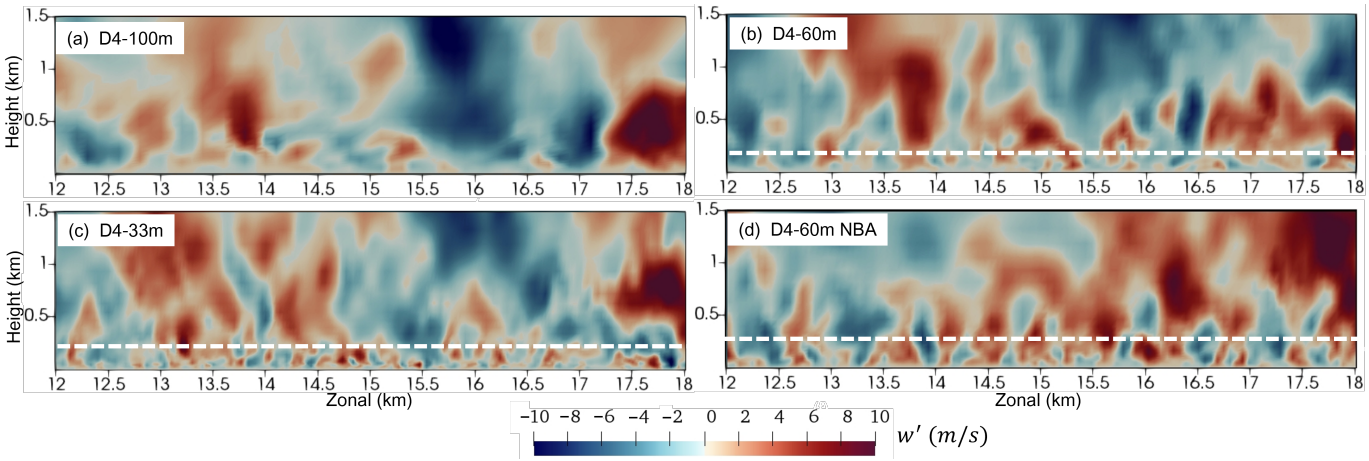

Figure 9. The vertical cross-section of w' (fluctuation component of the vertical velocity) at 0510UTC. The meridional coordinate of the cross-section is 33 km (the dashed line in Figure 8).

A vertical cross-section of the vertical velocity (Figure 9) illustrates this scale contrast more clearly. Below 200 m AGL, discernibly finer structures emerge as grid resolution increases, while above 200 m AGL, these fine-scale features become less distinct. This suggests that near-surface wind fluctuations are dominated by frictionally generated turbulence, whose resolved structures are sensitive to grid size. Notably, in D4-100 m, the scale of the dominant structures shows little variation with height (Figure 9a–c), indicating that a 100 m grid is insufficient to adequately resolve near-ground turbulence, consistent with findings obtained by Ito et al. [11], who also used Δx = 100 m. In the NBA run (D4-60 m NBA), the spacing between adjacent updraft and downdraft structures is visibly reduced compared with the TKE case, consistently with the horizontal patterns shown in Figure 8.

Moreover, the vertical extent of these fine-scale structures near the ground is slightly greater in the NBA simulation, implying enhanced vertical mixing.

Above 200 m AGL, the scale of the dominant fluctuations is similar across the D4 cases and thus less sensitive to grid resolution. Given their characteristic scale (about 1 km in the zonal direction), these features are likely consistent with HRSs within the TBL. Ito et al. [11] classified HRSs located outside the radius of maximum wind (e.g., 40 km away from the typhoon center in their study) as Type-A, oriented in the direction of the tangential wind. Such rolls are often associated with inflection-point instability in the radial velocity profile. In this study, the mean radial velocity profile within a 1.2 km × 1.2 km area around the Osaka AMeDAS at 0510 UTC was examined (Figure 10). The distance to the typhoon center (identified in D2) was approximately 38 km. An inflection point is evident in the profile of radial velocity for each D4 case (Figure 10a), located near 350 m AGL in all cases, consistent with the height at which large-scale fluctuation scales become similar.

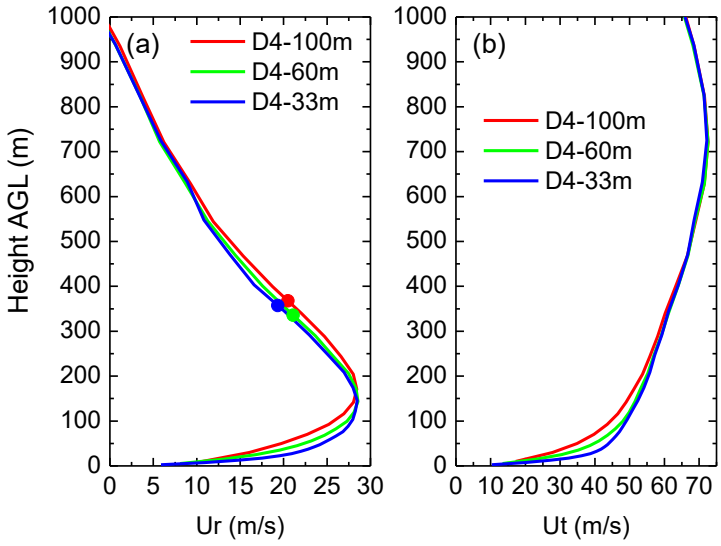

Figure 10. The vertical profiles of radial velocity (U_r, **a**) and tangential velocity (U_t, **b**) in D4 domains. The profiles are the mean profiles of the radial velocity in a 1.2 km × 1.2 km area around the Osaka AMeDAS at 0510UTC. The dots denote the inflection points of each profile.

A brief summary of the wind characteristics observed in this study in comparison with previous related work is provided below. The horizontal fluctuations with a scale of about 1 km observed in our simulations (e.g., Figure 8) are consistent with the HRSs (e.g., Type-A rolls) within the tropical cyclone boundary layer documented by Ito et al. [11]. The presence of an inflection point in the radial velocity profile (Figure 10a) further supports the dynamic instability mechanism for such rolls, aligning with the findings presented by Ito et al. [11] and others. The present result that a horizontal grid spacing of 100 m is sufficient to capture the organized roll structures, while a resolution of 60 m or less is needed to explicitly resolve smaller-scale turbulent streaks (Figure 8), is in qualitative agreement with the resolution threshold suggested by Liu et al. [19], who found that a resolution of about 100 m or less is necessary to simulate fine-scale coherent structures in the TBL.

3.4. Effective Mesh Resolution

The effective mesh resolution (EMR) is investigated to quantitatively assess the ability of WRF-LES to resolve turbulence. Following Skamarock [38], who defined EMR as the wavelength at which a simulated spectrum begins to decay relative to a reference spectrum (estimating it as $7\Delta x$ for mesoscale WRF), we adapt the concept for our high-resolution

LESs. Here, EMR is defined as the wavelength at which the computed spectrum begins to deviate from the theoretical $-5/3$ slope of the inertial subrange. It should be noted that at higher altitudes near the boundary-layer height (BLH), turbulence may not be fully developed, and the spectral cascade may not strictly follow the theoretical inertial subrange. In our simulation, the BLH is approximately 900–1000 m AGL, as indicated by the vertical extent of the turbulent stress profile (Figure 6c). However, this study focuses on turbulence in the lower part of the atmospheric boundary layer (below the BLH). Earlier studies support the applicability of the $-5/3$ slope within the TBL, for instance, at heights of 1011 m and 2069 m AGL, as shown by Green et al. [39], and at 370m AGL, as shown by Bi et al. [40]. Therefore, for consistency and simplicity, the $-5/3$ slope is retained as the reference for estimating the EMR even at higher levels within the analysis domain.

As noted, near-surface turbulence exhibits stripe-like patterns. Therefore, power spectra are computed from the fluctuating component of the northward wind (v') along the zonal direction. This approach is also suitable for higher levels where turbulence is more homogeneous. Figure 11a,b show that spectral energy at smaller wavelengths is significantly intensified near the ground but not at 350 m AGL. HRSs contribute to enhanced spectral energy at wavelengths around 1 km.

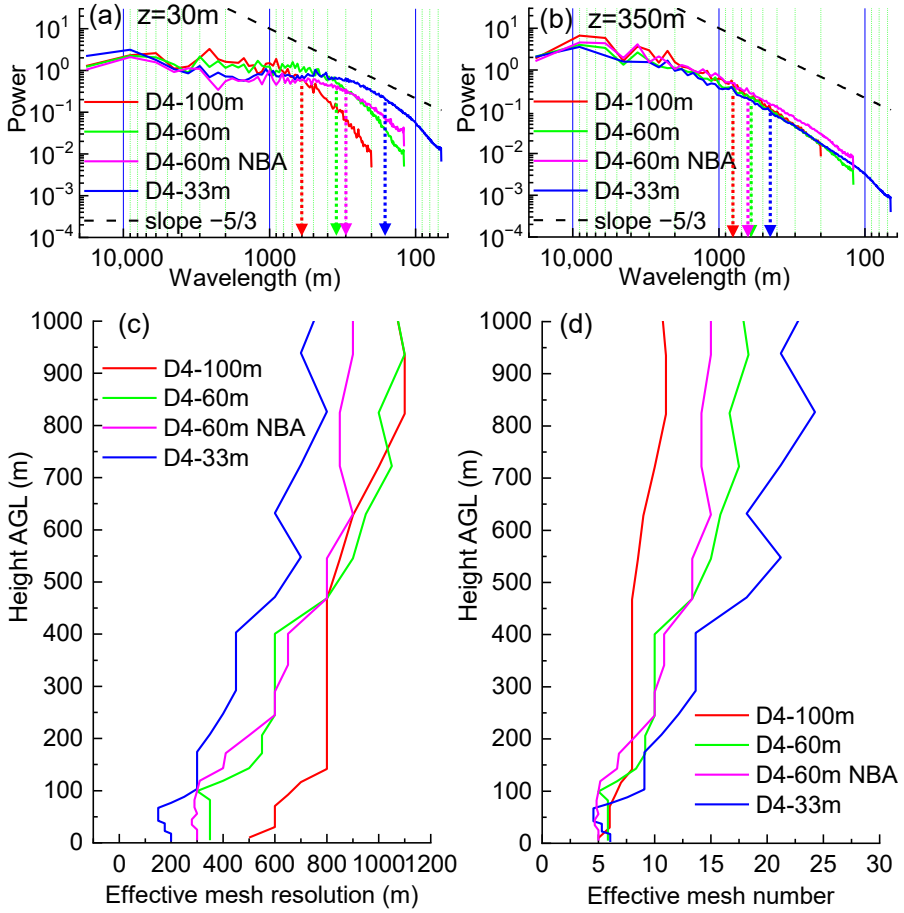

Figure 11. The spectra of v' in the zonal direction at (**a**) 30 m and (**b**) 350 m AGL. v' was sampled at the same location as in Figure 8 from 0505UTC to 0515UTC. The dashed lines show the estimated wavelength (EMR) at which the spectra begin to decay relative to the theoretical $-5/3$ slope. (**c**,**d**) The vertical profiles of the EMR and the corresponding mesh numbers.

The vertical profiles of the EMR (Figure 11c,d) indicate that near the surface, the effective resolution is approximately 5–9Δx, slightly finer than the 7Δx reported in several prior studies [4,7,38]. Above 100 m AGL, the EMR increases with height, suggesting a

reduction in resolved high-frequency content. It remains unclear whether this is due to coarser vertical resolution aloft. Above 500 m AGL, the EMR values for D4-100 m and D4-60 m converge (and are slightly larger than for D4-33 m), roughly matching the scale of the HRSs, consistently with the earlier observation that large-scale fluctuations are similar across cases. The NBA case yields a smaller EMR than the TKE case, particularly at low levels near the ground (approximately 300 m versus 350 m, respectively), consistently with the aforementioned finer-scale turbulent structures resolved by the NBA model. At higher altitudes (above about 300 m AGL), the difference in EMR between the two SGS models becomes negligible, suggesting that large-scale organized structures such as HRSs dominate the wind fluctuations aloft, irrespective of the SGS closure scheme.

Additional sensitivity tests were conducted for the D4-60 m configuration using the vertical grid spacings of D4-33 m and D4-100 m. Finer near-surface structures were generated with finer vertical resolution. Furthermore, for identical vertical grids, finer horizontal resolution also produced finer near-surface structures. This implies that both horizontal and vertical grid spacings constrain the scale of the finest resolvable turbulence.

4. Discussion

4.1. Main Findings and Contributions

This study confirms existing knowledge on the need for high resolution ($\leq$100 m) to resolve roll vortices in the tropical cyclone boundary layer [11,19] and on the tendency of the standard 1.5-order TKE SGS model to overshoot the near-surface wind profile under high-shear conditions [2]. Beyond these confirmations, the present work makes two primary novel contributions. First, it provides a quantitative evaluation of the SGS model performance under the strong-wind conditions of a real typhoon affecting an urban area. We demonstrate that the overshooting issue of the 1.5-order TKE model is amplified with finer grids and is significantly alleviated by the NBA model, which improves mean wind shear and yields finer near-surface turbulent structures (Figures 7–9). Second, the study quantifies the effective mesh resolution (EMR) for resolved turbulence near the surface in a real typhoon boundary layer (approximately 5–9 Δx) and highlights the role of upstream terrain undulation in turbulence generation (Figures 3 and 5). These findings extend previous research by clarifying how model physics, grid resolution, and local topography jointly shape near-surface wind characteristics during a high-impact typhoon.

Based on the results, we offer the following practical recommendations for implementing high-resolution WRF-LES in typhoon wind simulations:

1. Use a horizontal grid spacing of 60 m or less to explicitly resolve small-scale turbulent structures; a 100 m grid is sufficient for capturing horizontal roll vortices (HRSs).
2. Consider the NBA SGS model to improve the near-surface mean wind profile and the representation of fine-scale turbulence, as the standard TKE model tends to overestimate wind speeds.
3. When an accurate typhoon track is essential, apply spectral nudging in the outer domain to constrain large-scale biases, provided that high-resolution analysis data are available.

4.2. Limitations and Future Work

This study focused on Typhoon Jebi because it was a well-documented event that produced extreme winds in the Osaka region, offering a valuable test case for evaluating turbulence-resolving model performance under realistic strong-wind conditions. The analysis emphasizes physical process understanding, including turbulence spectra, roll vortices, and SGS model comparison, rather than statistical generalization. Although findings on grid sensitivity and SGS model behavior are likely relevant to other typhoons,

we recommend that future work include multiple typhoon cases to further assess the robustness and broader applicability of these results.

This study also did not include coupled ocean–atmosphere interactions. Ocean responses to typhoons, such as sea surface temperature cooling, mixed-layer deepening, and inertial currents, can modulate typhoon intensity and boundary-layer structure. For a detailed analysis of ocean responses to Pacific typhoons, readers may refer to recent work by Bernado et al. [41].

The high-resolution WRF-LES framework presented here can support practical engineering and planning projects, such as building wind load assessment, urban wind environment analysis, and localized wind field forecasting in typhoon-prone regions. By providing three-dimensional wind fields with resolved turbulent structures, the model can help improve the accuracy of related engineering designs and wind risk evaluations.

5. Conclusions

This study employed a high-resolution WRF-LES model to simulate Typhoon Jebi, which generated severe winds in Osaka. The performance of the model in resolving low-level wind characteristics within the TBL was evaluated. The main findings, structured around the key investigative themes, are summarized as follows:

1. Impact of geophysical parameters: High-frequency wind fluctuations were successfully resolved within the WRF-LES domains. Terrain undulations in the upstream region were found to promote turbulence generation.
2. Impact of the SGS model: The known shortcoming of the standard 1.5-order TKE SGS model, that is, to overshoot the near-surface wind profile due to insufficient turbulent stress, is confirmed in this typhoon case. The maximum nondimensional wind shear occurred near the second model level above the surface. A finer horizontal grid resolution tended to produce slightly larger wind shear. The NBA SGS model significantly reduced such overshoot and also resulted in finer-scale turbulent structures compared with the standard 1.5-order TKE SGS model.
3. Impact of spatial resolution: Finer turbulent structures were resolved with higher grid resolution. The effective mesh resolution near the surface was approximately 5–9 Δx, and a 100 m grid was sufficient to reproduce horizontal roll structures, but finer grids ($\leq$60 m) were necessary to explicitly resolve small-scale turbulent structures, particularly at low levels.

Author Contributions: Conceptualization, T.T.; methodology, T.T. and J.Z.; software, T.T. and J.Z.; validation, T.T., J.Z., B.H. and Q.Z.; formal analysis, T.T. and B.H.; investigation, T.T. and B.H.; resources, T.T.; data curation, T.T.; writing—original draft preparation, T.T.; writing—review and editing, T.T., J.Z., B.H. and Q.Z.; visualization, T.T. and B.H.; supervision, T.T.; project administration, T.T.; funding acquisition, T.T. All authors have read and agreed to the published version of the manuscript.

Funding: This research study was funded by the National Natural Science Foundation of China (52308474), the open funding of the Key Laboratory of Transport Industry of Wind Resistant Technology for Bridge Structures (KLWRTBMC24-01), the Innovation Team Project for Natural Sciences in Universities of Anhui Province (2024AH010005), the Research Start-up Fund for Talent Introduction of Anhui Polytechnic University (2023YQQ015), and the College Students' Innovative Entrepreneurial Training Plan Program (202410363118).

Institutional Review Board Statement: Not applicable.

Informed Consent Statement: Not applicable.

Data Availability Statement: The original contributions to the study are included in the article. The WRF configuration (the namelist.input file for the D4-60 m NBA case as an example) and the data for

drawing most figures in this manuscript can be found at the following link: https://doi.org/10.6084/m9.figshare.31044853. Further inquiries can also be directed to the corresponding author.

Conflicts of Interest: The authors declare no conflicts of interest.

Abbreviations

The following abbreviations are used in this manuscript:

WRF	Weather Research and Forecasting
LES	large-eddy simulation
TKE	turbulent kinetic energy
AGL	above ground level
NBA	nonlinear backscatter and anisotropy
TBL	typhoon boundary layer
HRS	horizontal roll vortex
PBL	planetary boundary layer
SGS	subgrid scale
YSU	Yonsei University
JMA	Japan Meteorological Agency
NCEP	National Centers for Environmental Prediction
GFS	Global Forecast System
RRTMG	Rapid Radiative Transfer Model for Global Climate Model
AMeDAS	Automated Meteorological Data Acquisition System
MB	mean bias
MAE	mean absolute error
RMSE	root mean square error
EMR	effective mesh resolution

References

1. Liu, Y.; Warner, T.; Liu, Y.; Vincent, C.; Wu, W.; Mahoney, B.; Swerdlin, S.; Parks, K.; Boehnert, J. Simultaneous nested modeling from the synoptic scale to the LES scale for wind energy applications. *J. Wind. Eng. Ind. Aerodyn.* **2011**, *99*, 308–319. [CrossRef]
2. Mirocha, J.; Lundquist, J.; Kosović, B. Implementation of a nonlinear subfilter turbulence stress model for large-eddy simulation in the Advanced Research WRF model. *Mon. Weather Rev.* **2010**, *138*, 4212–4228. [CrossRef]
3. Mirocha, J.; Kirkil, G.; Bou-Zeid, E.; Chow, F.K.; Kosović, B. Transition and equilibration of neutral atmospheric boundary layer flow in one-way nested large-eddy simulations using the weather research and forecasting model. *Mon. Weather Rev.* **2013**, *141*, 918–940. [CrossRef]
4. Mirocha, J.; Kosović, B.; Kirkil, G. Resolved turbulence characteristics in large-eddy simulations nested within mesoscale simulations using the Weather Research and Forecasting Model. *Mon. Weather Rev.* **2014**, *142*, 806–831. [CrossRef]
5. Kirkil, G.; Mirocha, J.; Bou-Zeid, E.; Chow, F.K.; Kosović, B. Implementation and evaluation of dynamic subfilter-scale stress models for large-eddy simulation using WRF. *Mon. Weather Rev.* **2012**, *140*, 266–284. [CrossRef]
6. Talbot, C.; Bou-Zeid, E.; Smith, J. Nested mesoscale large-eddy simulations with WRF: Performance in real test cases. *J. Hydrometeorol.* **2012**, *13*, 1421–1441. [CrossRef]
7. Rai, R.K.; Berg, L.K.; Kosović, B.; Mirocha, J.D.; Pekour, M.S.; Shaw, W.J. Comparison of measured and numerically simulated turbulence statistics in a convective boundary layer over complex terrain. *Bound.-Layer Meteorol.* **2017**, *163*, 69–89. [CrossRef]
8. Muñoz-Esparza, D.; Lundquist, J.K.; Sauer, J.A.; Kosović, B.; Linn, R.R. Coupled mesoscale-LES modeling of a diurnal cycle during the CWEX-13 field campaign: From weather to boundary-layer eddies. *J. Adv. Model. Earth Syst.* **2017**, *9*, 1572–1594. [CrossRef]
9. Foster, R.C. Why rolls are prevalent in the hurricane boundary layer. *J. Atmos. Sci.* **2005**, *62*, 2647–2661. [CrossRef]
10. Morrison, I.; Businger, S.; Marks, F.; Dodge, P.; Businger, J.A. An observational case for the prevalence of roll vortices in the hurricane boundary layer. *J. Atmos. Sci.* **2005**, *62*, 2662–2673. [CrossRef]
11. Ito, J.; Oizumi, T.; Niino, H. Near-surface coherent structures explored by large eddy simulation of entire tropical cyclones. *Sci. Rep.* **2017**, *7*, 3798. [CrossRef]
12. Yoshino, K. Low-level wind shear induced by horizontal roll vortices at Narita International Airport, Japan. *J. Meteorol. Soc. Japan Ser. II* **2019**, *97*, 403–421. [CrossRef]

13. Cao, S.; Tamura, Y.; Kikuchi, N.; Saito, M.; Nakayama, I.; Matsuzaki, Y. Wind characteristics of a strong typhoon. *J. Wind. Eng. Ind. Aerodyn.* **2009**, *97*, 11–21. [CrossRef]
14. Nakayama, H.; Takemi, T.; Nagai, H. Large-eddy simulation of urban boundary-layer flows by generating turbulent inflows from mesoscale meteorological simulations. *Atmos. Sci. Lett.* **2012**, *13*, 180–186. [CrossRef]
15. Yoshida, T.; Takemi, T. Properties of mixing length and dispersive stress in airflows over urban-like roughness obstacles with variable height. *Sola* **2018**, *14*, 174–178. [CrossRef]
16. Takemi, T.; Yoshida, T.; Yamasaki, S.; Hase, K. Quantitative estimation of strong winds in an urban district during Typhoon Jebi (2018) by merging mesoscale meteorological and large-eddy simulations. *Sola* **2019**, *15*, 22–27. [CrossRef]
17. Tao, T.; Tamura, T. Numerical study of the 6 May 2012 Tsukuba supercell tornado: Vorticity sources responsible for tornadogenesis. *Mon. Weather Rev.* **2020**, *148*, 1205–1228. [CrossRef]
18. Zhu, P. Simulation and parameterization of the turbulent transport in the hurricane boundary layer by large eddies. *J. Geophys. Res. Atmos.* **2008**, *113*.. [CrossRef]
19. Liu, Q.; Wu, L.; Qin, N.; Li, Y. Storm-scale and fine-scale boundary layer structures of tropical cyclones simulated with the WRF-LES framework. *J. Geophys. Res. Atmos.* **2021**, *126*, e2021JD035511. [CrossRef]
20. Wyngaard, J.C. Toward numerical modeling in the "Terra Incognita". *J. Atmos. Sci.* **2004**, *61*, 1816–1826. [CrossRef]
21. Takahashi, T.; Nolan, D.S.; McNoldy, B.D. The vortex structure and near-surface winds of Typhoon Faxai (2019) during landfall. Part II: Evaluation of WRF simulations. *Q. J. R. Meteorol. Soc.* **2024**, *150*, 1643–1667. [CrossRef]
22. Zhang, Y.; Cao, S.; Cao, J. A framework for efficient simulation of urban strong wind field during typhoon process using coupled WRF-UCM and embedded LES model. *J. Wind. Eng. Ind. Aerodyn.* **2024**, *250*, 105757. [CrossRef]
23. Zhao, Z.; Xiao, Y.; Li, C.; Chan, P.; Hu, G.; Zhou, Q. Multiscale simulation of the urban wind environment under typhoon weather conditions. *Build. Simul.* **2023**, *16*, 1713–1734. [CrossRef]
24. Skamarock, W.C.; Klemp, J.B. A time-split nonhydrostatic atmospheric model for weather research and forecasting applications. *J. Comput. Phys.* **2008**, *227*, 3465–3485. [CrossRef]
25. Hong, S.Y.; Noh, Y.; Dudhia, J. A new vertical diffusion package with an explicit treatment of entrainment processes. *Mon. Weather Rev.* **2006**, *134*, 2318–2341. [CrossRef]
26. Deardorff, J. A three-dimensional numerical study of turbulent channel flow at large Reynolds numbers. *J. Fluid Mech.* **1970**, *41*, 453–480. [CrossRef]
27. Chu, X.; Xue, L.; Geerts, B.; Rasmussen, R.; Breed, D. A case study of radar observations and WRF LES simulations of the impact of ground-based glaciogenic seeding on orographic clouds and precipitation. Part I: Observations and model validations. *J. Appl. Meteorol. Climatol.* **2014**, *53*, 2264–2286. [CrossRef]
28. Markowski, P.M.; Bryan, G.H. LES of laminar flow in the PBL: A potential problem for convective storm simulations. *Mon. Weather Rev.* **2016**, *144*, 1841–1850. [CrossRef]
29. Xue, L.; Chu, X.; Rasmussen, R.; Breed, D.; Geerts, B. A case study of radar observations and WRF LES simulations of the impact of ground-based glaciogenic seeding on orographic clouds and precipitation. Part II: AgI dispersion and seeding signals simulated by WRF. *J. Appl. Meteorol. Climatol.* **2016**, *55*, 445–464. [CrossRef]
30. National Centers for Environmental Prediction, National Weather Service, NOAA, U.S. Department of Commerce. NCEP GFS 0.25 Degree Global Forecast Grids Historical Archive. 2015. Available online: https://gdex.ucar.edu/datasets/d084001/ (accessed on 4 September 2018).
31. Hashimoto, S.; Tadono, T.; Onosato, M.; Hori, M.; Shiomi, K. A new method to derive precise land-use and land-cover maps using multi-temporal optical data. *J. Remote Sens. Soc. Jpn.* **2014**, *34*, 102–112.
32. Morrison, H.; Thompson, G.; Tatarskii, V. Impact of cloud microphysics on the development of trailing stratiform precipitation in a simulated squall line: Comparison of one-and two-moment schemes. *Mon. Weather Rev.* **2009**, *137*, 991–1007. [CrossRef]
33. Iacono, M.J.; Delamere, J.S.; Mlawer, E.J.; Shephard, M.W.; Clough, S.A.; Collins, W.D. Radiative forcing by long-lived greenhouse gases: Calculations with the AER radiative transfer models. *J. Geophys. Res. Atmos.* **2008**, *113*. [CrossRef]
34. Chen, F.; Dudhia, J. Coupling an advanced land surface–hydrology model with the Penn State–NCAR MM5 modeling system. Part I: Model implementation and sensitivity. *Mon. Weather Rev.* **2001**, *129*, 569–585. [CrossRef]
35. Jiménez, P.A.; Dudhia, J.; González-Rouco, J.F.; Navarro, J.; Montávez, J.P.; García-Bustamante, E. A revised scheme for the WRF surface layer formulation. *Mon. Weather Rev.* **2012**, *140*, 898–918. [CrossRef]
36. Brasseur, J.G.; Wei, T. Designing large-eddy simulation of the turbulent boundary layer to capture law-of-the-wall scaling. *Phys. Fluids* **2010**, *22*, 021303. [CrossRef]
37. Kosović, B. Subgrid-scale modelling for the large-eddy simulation of high-Reynolds-number boundary layers. *J. Fluid Mech.* **1997**, *336*, 151–182. [CrossRef]
38. Skamarock, W.C. Evaluating mesoscale NWP models using kinetic energy spectra. *Mon. Weather Rev.* **2004**, *132*, 3019–3032. [CrossRef]

39. Green, B.W.; Zhang, F. Numerical simulations of hurricane katrina (2005) in the turbulent gray zone. *J. Adv. Model. Earth Syst.* **2015**, *7*, 142–161. [CrossRef]
40. Bi, X.; Lu, C.; Liu, C.; Huang, J.; Yang, H.; Zhao, Z.; Song, Q. Comparison of Atmospheric Turbulence Characteristics over Sea Surface and Land Surface before, during, and after Typhoons. *Atmosphere* **2022**, *13*, 1827. [CrossRef]
41. Bernado, A.; Belonenko, T.; Budyansky, M. Ocean response to Pacific typhoons passing in extratropical latitudes. *Sovremennye Problemy Distantsionnogo Zondirovaniya Zemli iz Kosmosa [Curr. Probl. Remote Sens. Earth Space]* **2025**, *22*, 254–267.